DOI: 10.13009/EUCASS2022-6142
9TH EUROPEAN CONFERENCE FOR AERONAUTICS AND SPACE SCIENCES (EUCASS)

Influence of Physical Models on the Numerical Modeling of Hypersonic Nozzle Flow Expansion

Matthias Geratz⋆, Michele Capriati⋆, Guillaume Grossir⋆ and Thierry E. Magin⋆
⋆ von Karman Institute for Fluid Dynamics
Waterloosesteenweg 72, 1640 Sint-Genesius-Rode (BE)

Abstract

The flow expansion through the Longshot hypersonic contoured nozzle is simulated with the US3D code. The Spalart-Allmaras turbulence model with compressibility correction is employed. High-pressure effects are modeled by the excluded volume equation of state. Vibrational excitation of the nitrogen gas is accounted for by either a thermal equilibrium or two-temperature approach. The real gas corrections exhibit significant influence on the flow expansion and free-stream quantities. Vibrational freezing is predicted to take place shortly after the nozzle throat. Comparisons with Pitot pressure measurements indicate that the free-stream Mach number and the boundary layer thickness are considerably overestimated by the simulations.

1. Introduction

In spite of the continuous advance of numerical capabilities, hypersonic wind tunnels still remain important cornerstones for the development of the next generation of aerospace vehicles [24]. These advanced facilities provide a controlled environment in which numerous investigations can be conducted. As such, they represent an important link between numerical modeling and real-world applications by providing valuable validation data. Furthermore, they are a cost-effective alternative to flight tests. Many of these hypersonic facilities have been operated for decades. Yet, the fine characterization of their free-stream remains a challenging feat and continuous efforts are being expended to improve the understanding of the nozzle flow expansion, and the determination of the free-stream flow conditions. Ultimately, this can benefit the quality of the reference data acquired in these ground facilities.
One such hypersonic installation is the von Karman Institute's Longshot gun tunnel [29, 15], depicted in Figure 1. This cold hypersonic wind tunnel enables the simulation of reentry flow conditions at large Mach numbers and large Reynolds numbers as experienced during real reentries.

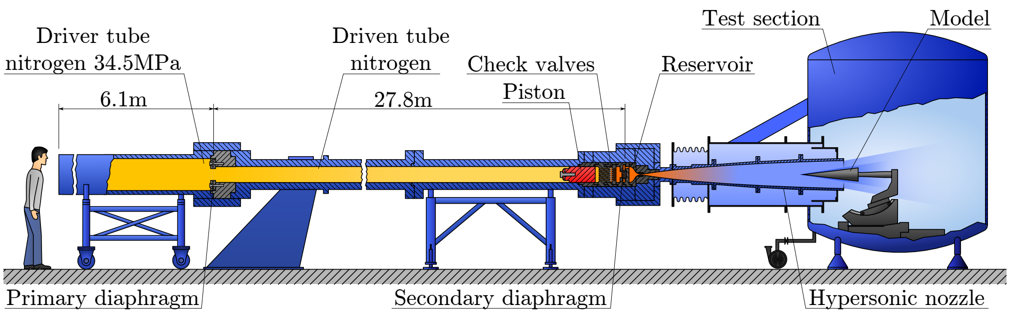

Figure 1: Sketch of the VKI Longshot hypersonic gun tunnel [12].

An inertial piston is used to compress the test gas to large stagnation pressures (up to 400 MPa) and large stagnation temperature (up to 3000 K). The generation of these stagnation conditions is governed by the piston mass and initial gas pressures in both driver and driven tubes. The test gas is then expanded through one of the three currently available nozzles to achieve the desired free-stream flow conditions.
In the following, emphasis is placed on the analysis of the nitrogen flow expansion through the most recent contoured nozzle, designed, manufactured and commissioned in 2019 [23]. This nozzle has been designed with the method of characteristics using the VKI Hypnoze design tool [13], accounting for both high-pressure and high-temperature effects and featuring an appropriate viscous correction derived from numerical results. The design operating conditions of this

DOI: 10.13009/EUCASS2022-6142

nozzle are 166 MPa and 2400 K for its stagnation pressure and temperature, respectively, resulting in a stagnation enthalpy of 3.020 MJ/kg using the NIST reference equation of state [36]. This axisymmetric contoured nozzle was designed for Mach 18. It is 4 m long and is characterized by an exit diameter of 541 mm. Typical useful test times are on the order of 20 ms.

The free-stream flow characterization in the Longshot tunnel relies on intrusive probes [17] placed in the free-stream and follows the method described in [12]. Great confidence has been achieved in the determination of the free-stream flow conditions, and confirmed with several independent measurement techniques [14]. Yet, the free-stream Mach number measured by the nozzle exit (about 14) [23] significantly differs from the design value of the nozzle (Mach 18). Other free-stream flow properties (static pressure, static temperature) are influenced and are actually the root for this lower free-stream Mach number. This relates to unexpected heating of the flow during the expansion process, leading to a non-isentropic flow expansion, although the exact mechanism(s) for these observed discrepancies remains unknown to date.

In this work, we investigate the nozzle flow expansion from a numerical point of view, aiming at obtaining a better physical understanding of the expansion through the use of advanced physical models. For this purpose, steady state simulations of the Longshot nozzle flow expansion are performed using the state-of-the-art hypersonic flow solver US3D [6]. We account for turbulence, high-temperature effects, dense gas effects, and thermal non-equilibrium effects. The corresponding predictions are compared with reference Pitot pressure measurements performed by Kovács et al. [23] at several locations along the nozzle. The deviations observed between experimental data and numerical results serve as a basis for a discussion of the mechanisms possibly at play. Lastly, the need for further investigations is established.

2. Simulation setup

This section introduces all the necessary components for the numerical solution of the hypersonic nozzle flow. The simulations are performed with the US3D simulation software [6]. All physical models and numerical schemes investigated are enabled by configuring the input parameters of the US3D solver. In the following, the employed physical models, numerical schemes and boundary conditions are enumerated. Furthermore, the relevant high-pressure and high-temperature modifications to the gas equations of state and energy are introduced. Generation procedures for the grid and initial conditions are presented. Lastly, the simulation methodology and convergence results are discussed.

2.1 Governing equations

The fundamental governing equations of a hypersonic flow are the compressible Navier-Stokes equations. Additionally, a gas equation of state is required as a closure to compute the pressure. Further equations are added to account for real gas and turbulence effects. In general, the methods and equations used are detailed by Candler in [5]. In the following, we outline the main model choices.

Due to the extreme stagnation pressures involved, the boundary layers are assumed to be fully turbulent all along the nozzle walls. Therefore, the compressible Reynolds Averaged Navier-Stokes (RANS) equations are solved. Species quantities, such as the laminar viscosity, are given by the Blottner curve fits [3]. To compute the turbulent viscosity, the one-equation Spalart-Allmaras turbulence model [35] with the compressible correction developed by Catris and Aupoix [8] (SA-Catris) is chosen as it was found to yield good results for similar problems [5].

Due to the extreme pressure in the reservoir and at the nozzle throat, the ideal gas equation of state exhibits significant error compared to more accurate alternatives, such as the Van-der-Waals equation. The Van-der-Waals equation extends the ideal gas equation by adding two high-pressure corrections. Accounting only for the correction due to the molecular volume in the Van-der-Waals equation and neglecting the second correction yields the excluded volume equation of state [5]:

$$p = \frac{\rho R_s T}{1 - \rho b}, \tag{1}$$

with specific gas constant $R_s = R/M$ and Van-der-Waals co-volume constant b. We only consider pure nitrogen, for which the molecular weight is $M = 28.01340\,\mathrm{kg/kmol}$ [9] and the co-volume is taken as $b = 0.00138148\,\mathrm{m^3/kg}$ [18]. With the general gas constant R given by [37], the specific gas constant for nitrogen is approximately equal to $R_{N_2} \approx 296.803\,\mathrm{J/(kg\,K)}$. These quantities are needed to compute the enthalpy for a given temperature and pressure. Since the co-volume term corrects the ideal gas equation for the volume of the gas molecules, the simulation cases performed using the excluded volume equation of state are also denoted by "volume correction" in the following.

To quantify the strength of the high-pressure effects the compressibility factor Z is used, which is defined as [5]:

DOI: 10.13009/EUCASS2022-6142

$$Z = \frac{p}{\rho R_{N_2} T}. \tag{2}$$

The compressibility factor "measures the departure of the dense gas from the perfect gas equation of state" [5]. For an ideal gas the compressibility factor is by design always equal to one. Using the volume correction, the compressibility factor can be written as $Z = 1/(1 - \rho b)$, which is always greater than one. Therefore, the excluded volume equation of state yields smaller densities than the ideal gas equation of state for a given pressure and temperature. The larger Z, the more influential high-pressure effects become.

In addition to the high-pressure correction, the reservoir temperature is also high enough for the gas to deviate from calorically perfect behavior, requiring a high-temperature correction. For the temperature ranges present in the Longshot nozzle, the high-temperature correction consists of accounting for the vibrational excitation of the diatomic nitrogen molecules. Together with the translational-rotational internal energy of a calorically perfect gas with constant heat capacity, the vibrational excitation results in greater heat capacity at higher temperatures. Therefore, the specific internal energy becomes a nonlinear function with respect to the temperature.
Furthermore, the exchange of energy between the translational-rotational and vibrational modes is a finite rate process which can take a significant amount of time with respect to the characteristic time of the nozzle flow expansion. Hence, we consider a thermal equilibrium model and a non-equilibrium two-temperature model in this work. Assuming sufficiently fast relaxation times, the thermal equilibrium model simply uses a function of a single temperature T_{eq} for the internal energy that accounts for the non-constant heat capacity. Dropping the equilibrium assumption leads to the two-temperature approach, where a conservation equation for the vibrational energy is added to the RANS equation system. The vibrational energy is characterized by a vibrational temperature T_{vib} separate from the translational-rotational temperature T_{tr}. The vibrational temperature is equal to the equilibrium temperature of a given vibrational energy. As described in [5], the exchange between the two energy modes is computed with the Landau-Teller rate model [2] with relaxation times given by Millikan and White [27, 28]. Note that the relaxation time is inversely proportional to the pressure and temperature. Therefore, the relaxation time increases exponentially during the flow expansion, quickly reaching a point at which the vibrational energy equation decouples from the equation system.
For the presented high-pressure and high-temperature corrections, the specific total enthalpy is given by:

$$\begin{aligned} h_{tot} &= u + \frac{p}{\rho} \\ &= h_{tr} + h_{kin} + h_p + h_{vib} \\ &= c_{p,tr} T + \frac{\vec{v}^{\,2}}{2} + pb + e_v, \end{aligned} \tag{3}$$

where u is the internal energy, $c_{p,tr} = 7/2\, R_{N_2}$ is the translational-rotational contribution to the heat capacity at constant pressure and e_v is the vibrational energy. One contribution each for the high-pressure and high-temperature models is added to the ideal gas calorically perfect enthalpy $h_{tr} + h_{kin}$. The pressure term $h_p = pb$ stems from substituting the excluded volume equation of state (1) into the p/ρ term of the enthalpy. For the thermal equilibrium case, the vibrational enthalpy $h_{vib} = e_v$ is obtained by subtracting the calorically perfect internal energy from the total internal energy $u(T)$, which is computed using the NASA Lewis curve fits. In the two-temperature case, the curve fits are used to find T_{vib} for a given e_v. Lastly, the reference enthalpy is at zero Kelvin, i.e., $h(T = 0) = 0$.

The presented models are simulated with US3D [6] configured to use implicit Euler time integration and modified Steger-Warming flux vector splitting derived by Candler in [5].

2.2 Grid generation

The two-dimensional axial slice of the axisymmetric nozzle is discretized with 100 cells in radial y-direction and 1000 cells in axial x-direction. On the initial grid a potential flow problem through the nozzle, described by a Laplace equation, is solved. The existing vertical grid lines are replaced with the computed vertical equipotential lines, which are orthogonal to the wall. Furthermore, by choosing a linear spacing of the potential values, the horizontal spacing between the lines is proportional to the nozzle radius, resulting in strong grid refinement at the throat region. The vertical cell spacing of a given line is determined by geometric growth with a growth factor of 1.2 and a wall cell size of $5 \cdot 10^{-7}$ times the local radius. This yields a dimensionless wall distance y^+ of less than $1/2$ for all considered cases. Since US3D solves in three dimensions, the 2D grid is extruded to three dimensions by rotation around the axis by one degree and translation by 10^{-10} m in z-direction to avoid overlapping cell edges at the axis. The resulting single cell deep wedge mesh is then used for axisymmetric simulations.

DOI: 10.13009/EUCASS2022-6142

2.3 Initialization conditions

To increase convergence speed and especially stability the simulation is initialized with a quasi-1D isentropic nozzle flow. An equation system of enthalpy, entropy and mass conservation closed with the gas equation of state is numerically solved to compute discrete distributions of all fluid flow variables. The state variables only depend on the cross-sectional area, which is given by the contour function. Together with the contour function, the prescribed reservoir enthalpy and pressure are used to define the constant values of the three conserved quantities. The mass flow rate is determined using the critical state at the throat. For the cases using high temperature corrections, Mutation++ [33] is employed to compute the entropy and vibrational energy.

Although accounting for the real gas effects in the initialization conditions does not significantly increase stability, using matching models helps with convergence speed, due to the inflow and initialization conditions being consistent. Moreover, the code is used to calculate the correct inflow conditions for the various gas models.

2.4 Boundary conditions

The US3D solver is configured with suitable boundary conditions for the hypersonic nozzle flow expansion problem. For the axisymmetric simulation using the wedge mesh, symmetry boundary conditions are prescribed at all front, back and axial faces. The outflow is set to supersonic outflow conditions. For the nozzle wall, an isothermal boundary condition with $T_{\text{wall}} = 300\,\text{K}$ is chosen, justified by the short test times achieved in the tunnel, although local departure from this simplifying assumption could occur in the throat region where the largest heat transfer is expected.

Two possible choices exist for the inflow boundary condition. Firstly, the reservoir temperature, pressure and inflow velocity can be prescribed with a subsonic inflow condition. Alternatively, a velocity inlet condition, where the inflow velocity, temperature and density are prescribed, can be applied. For the tested cases, both approaches yield the same flow field. Note, that the thermal equilibrium case requires the velocity inlet condition. Furthermore, since stability and convergence speed are higher for the velocity inlet condition, it is chosen for the presented results.

The values of the inflow temperature, density and velocity are taken from the initialization conditions and shown in Tables 1, 2 and 3 respectively. The four entries in the tables correspond to the possible combinations of the pressure treatment by the equation of state and the temperature treatment with the vibrational energy. Note that the two-temperature case is assumed to be in thermal equilibrium in the reservoir, thus it has the same inflow conditions as the equilibrium case.

For comparison purposes among the different test cases with different physical models, the reservoir enthalpy and pressure are kept constant for all cases. They are chosen equal to the nozzle design enthalpy (3.020 MJ/kg) and pressure (166 MPa), since that is the most important case. The reservoir enthalpy is chosen constant across the cases rather than the temperature, because direct reservoir temperature measurements are not available. Hence, the reservoir temperatures are deduced using the measured reservoir pressure and flow total enthalpy computed from free-stream measurements. Depending on the model, a portion of the enthalpy is bound in the correction terms, thus the temperature and consequently density varies drastically between the cases, as seen in Tables 1 and 2. Using both the volume correction and high-temperature model, the temperature is lower than the 2400 K design temperature, since the excluded volume equation of state overestimates the pressure-enthalpy. More accurate temperatures can be achieved by using the full Van-der-Waals equation of state.

Table 1: Inflow temperature

	ideal gas	**high-pressure correction**
calorically perfect	2907.21 K	2686.45 K
high-temperature correction	2544.49 K	2368.81 K

Table 2: Inflow density

	ideal gas	**high-pressure correction**
calorically perfect	192.381 kg/m^3	161.687 kg/m^3
high-temperature correction	219.806 kg/m^3	178.035 kg/m^3

DOI: 10.13009/EUCASS2022-6142

Table 3: Inflow velocity

	ideal gas	**high-pressure correction**
calorically perfect	1.50070 m/s	1.71147 m/s
high-temperature correction	1.36645 m/s	1.59249 m/s

2.5 Simulation methodology

To investigate the influence of the individual model choices, all six combinations arising from the two pressure and three temperature treatments are simulated. In the following, the gas equation of state used is denoted by either "ideal" or "volume correction" while the temperature models are denoted by "calorically perfect", "thermal equilibrium" or "two-temperature".

At the start of the simulation the CFL number is low and then ramped up to ensure stability. To reach a steady state within reasonable time, the CFL number is chosen as large as possible without the simulation crashing. It is observed that the CFL number is proportional to the root mean square density residual that is achieved, meaning that for large CFL numbers the residual does not decrease much from its initial value. Lowering the CFL number will reduce the residual by several orders of magnitude, yet convergence up to machine precision remains out of reach. The large residual originates from oscillations in the solution variables present in cells that are close to the wall. Although a majority of the unsteady behavior is therefore confined to a limited region, the influence of this region causes slight variations in the free-stream quantities over time.

Since the simulations do not converge, special care is taken to ensure a steady state solution has been reached. Because some quantities, such as the Mach number, converge faster to a steady state than others, such as the total enthalpy, a solution may appear steady while large errors in relevant quantities still exist. For this reason, both the Mach number and enthalpy are visually compared for multiple sufficiently apart instances in time to guarantee a steady solution. The maximum relative difference of the enthalpy along the axis is 1.000479, thus for all cases the enthalpy variation along the axis is smaller than 0.05%.

The slight unsteady variations in the free-stream quantities prohibit the calculation of the grid convergence index [32], thus making error estimation difficult. This is because the grid convergence index requires the discretization error to be the dominant error [11], which is not the case. Therefore, the asymptotic order of convergence determined by means of systematic grid refinement [11] varies greatly with time, making the error estimation difficult. Nonetheless, refining and coarsening the grid both result in only marginally different free-stream quantities, indicating sufficiently accurate results for the comparisons and conclusions drawn in this work.

3. Simulation results

The Longshot compression cycle with an inertial piston leads to the generation of large stagnation pressures and temperatures, up to 400 MPa and 2500 K, respectively. The large stagnation temperature generated, and the large number of collisions taking place, excite the nitrogen vibrationally, leading to a calorically imperfect gas behavior. Furthermore, the dense gas effects taking place at these conditions justifies the need for an excluded volume equation of state in the following simulations.

The nitrogen test gas that is compressed in the reservoir is then rapidly accelerated to hypersonic Mach numbers using the contoured shape nozzle. This flow expansion is associated with a rapid decrease of the static pressure and static temperature of the gas, which possibly leads to thermal non-equilibrium effects as a result of the reduced number of collisions between the molecules and the rapidly changing thermodynamic state of the gas.

The specific geometry of this 4 m long contoured nozzle enables to generate a parallel flow by the exit (as opposed to the residual divergent flow that would be obtained with conical nozzles). The residual divergence of the nozzle walls by the nozzle exit only serves to compensate for the rapidly growing hypersonic boundary layers along the nozzle walls. These boundary layers are expected to be fully turbulent all along the nozzle contour. Indeed, the large stagnation pressure involved leads to extremely thin boundary layers in the vicinity of the nozzle throat region. Any wall surface roughness, however small, is then expected to by-pass the natural boundary layer laminar-to-turbulent transition phenomena and to promote the transition to turbulence of the nozzle wall boundary layers as from the throat region.

With this general overview in mind, the six cases arising from the combination of the two gas equations of state and the three temperature models are compared to each other to evaluate the influence of physical model choices on the nozzle flow expansion. Furthermore, we assess whether these kinds of models have the capability to explain the experimentally

DOI: 10.13009/EUCASS2022-6142

measured free-stream conditions. For this purpose, the simulation results are postprocessed using US3D [6], Paraview [1], Matlab [26], and visualized using Gnuplot [38].

3.1 Influence of dense gas effects

The magnitude of the dense gas effects is characterized by the compressibility factor Z, defined in Equation (2). Its variations in the vicinity of the throat region are plotted in Figure 2a for all three cases that use the excluded volume equation of state (Eq. (1)). Important deviations from the ideal gas law are observed in the reservoir ($Z = [1.29{-}1.325]$), and in the throat region ($Z = [1.17 - 1.19]$), due to the large pressures involved in these regions. The compressibility factor then rapidly drops to about 1 shortly after the throat ($Z = [1.0013 - 1.0014]$ for $x = 0.1$ m), hence very quickly approaching an ideal gas behavior in the inviscid region. The fact that the compressibility factor is lower in the calorically perfect case (excluding high-temperature effects), is a consequence of the greater temperatures (therefore lower density) occurring for the prescribed design enthalpy.

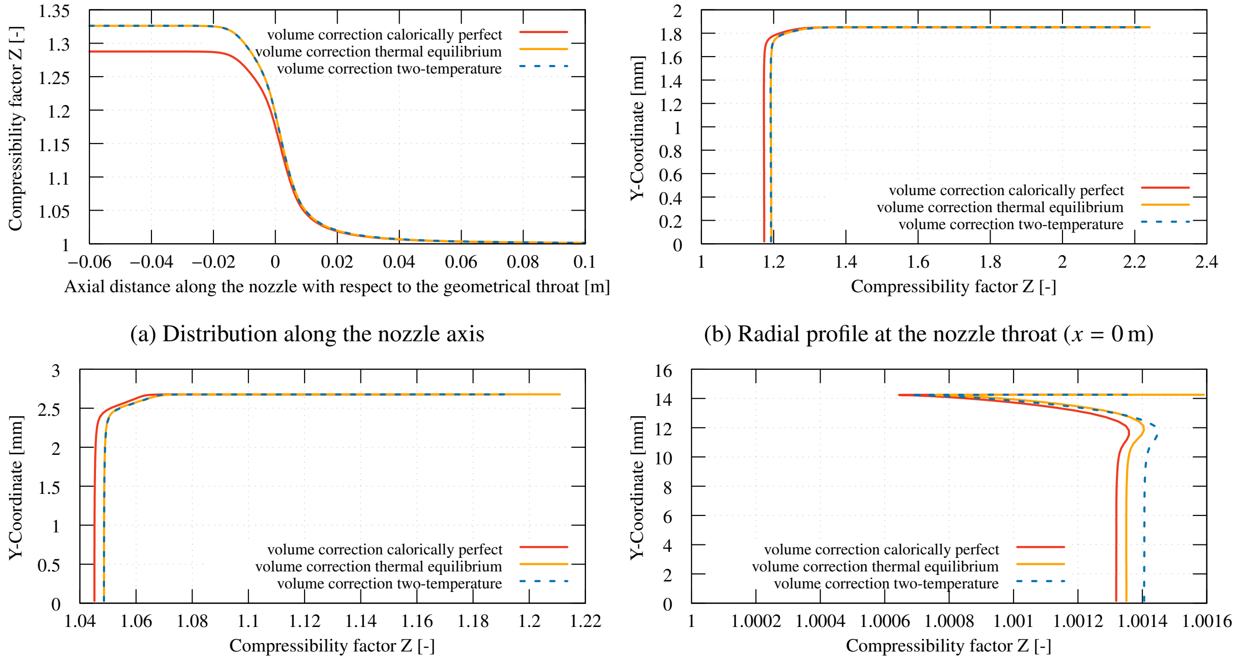

(a) Distribution along the nozzle axis

(b) Radial profile at the nozzle throat ($x = 0$ m)

(c) Radial profile at $x = 0.01$ m

(d) Radial profile at $x = 0.1$ m

Figure 2: Compressibility factor $Z = p/(\rho R_{N_2} T)$ for the three cases using the excluded volume equation of state.

Closer to the wall within the boundary layers, the compressibility factor is larger than in the core flow (and even much larger than the values reported in the reservoir) as shown in Figures 2b and 2c. This is the result of the cool nozzle surfaces (assumed to remain at ambient temperature as a result of the short test times typically achieved in the tunnel) as opposed to the larger gas temperatures that exist farther from the wall surfaces. The evolution of the radial profiles (2b, 2c, 2d) shows the compressibility factor quickly decreasing in the entire nozzle diameter (even close to the wall) as the gas expands, approaching ideal gas behavior.
Overall, the non-negligible compressibility factors observed within the reservoir and in the vicinity of the throat across the whole flow profile demonstrate that the use of an excluded equation of state is required for an accurate simulation of the Longshot nozzle flow expansion.

3.2 Influence of thermal non-equilibrium effects

The rapid flow expansion that takes place in the vicinity of the throat is associated with a large drop of the number of collisions in between the molecules, possibly leading to thermal non-equilibrium effects. This would result in a different temperature distribution along the nozzle with respect to an equilibrium flow expansion.
Figure 3 compares the temperatures of the flow for the equilibrium and two-temperature models when using the volume correction. Within 10 mm beyond the throat location, the vibrational temperature of the nitrogen departs from the translational-rotational temperature (as can be seen in the close up in Figure 3a) and remains frozen for the rest of the

DOI: 10.13009/EUCASS2022-6142

expansion (T_v = 1818 K). The conservation of the total enthalpy requires that the translational-rotational temperature falls below the equilibrium temperature. A logarithmic scale is used for the temperature axis to clearly show the difference between the predicted equilibrium temperature and the translational-rotational temperature of the two-temperature model. The axial temperature at the nozzle exit is decreased from $T_{eq} \approx 44.9$ K to $T_{rt} \approx 37.6$ K when switching from the thermal equilibrium to the two-temperature model. Vibrational freezing also influences other flow quantities along the expansion, the flow velocity being typically reduced by 77 m/s at the axis by the nozzle exit with respect to a thermal equilibrium expansion, while the static pressure is reduced by roughly 9 % for the conditions studied herein.

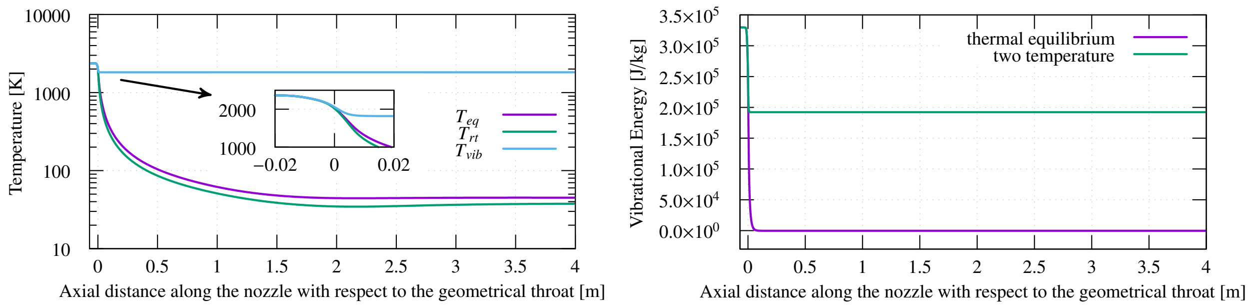

(a) Temperatures along the axis

(b) Vibrational energies along the axis

Figure 3: Comparison of the temperatures (a) and vibrational energies (b) of the equilibrium and two-temperature models using the excluded volume equation of state.

Radial profiles of the vibrational energy are plotted in Figure 4 for both high-temperature models when using the volume correction. At the wall the vibrational energy drops to zero for both cases due to the prescribed ambient temperature along the entire wall. The two-temperature profile departs from the thermal equilibrium profile as the flow expands and the vibrational energy freezes. Even in the boundary layer, the vibrational energy remains frozen, as can be seen in Figure 4b. The decrease in frozen vibrational energy in the viscous region is attributed mainly to the advection of the initial profile rather than relaxation. Under the thermal equilibrium assumption, the vibrational energy relaxes to zero in the inviscid region, while inside the boundary layer a small peak remains. Corresponding to about 0.45 % of the local total enthalpy, this peak is caused by the elevated temperature inside the boundary layer. How much impact this has on the boundary layer and subsequently on the flow expansion remains unclear.

Generally, the presence of significant amounts of vibrational energy in the reservoir and throat regions necessitates the use of high-temperature models and consideration of thermal non-equilibrium for the accurate description of the flow expansion in the Longshot nozzle.

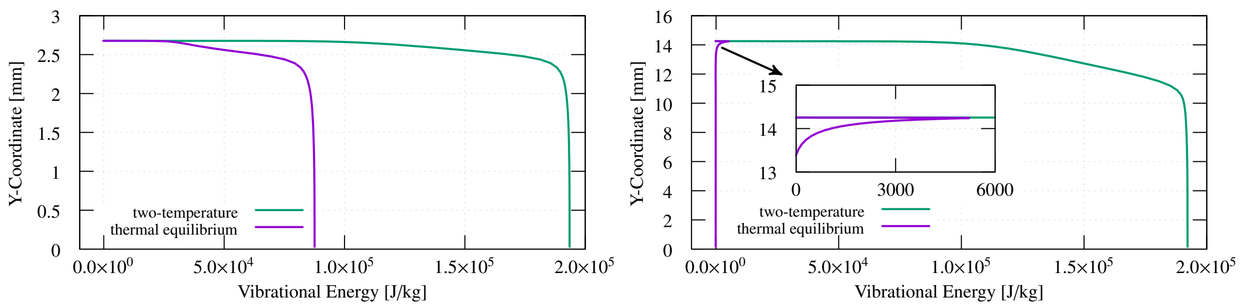

(a) Vibrational energies radial profile at x = 0.01 m

(b) Vibrational energies radial profile at x = 0.1 m

Figure 4: Radial profiles of the thermal equilibrium and two-temperature vibrational energies using the excluded volume equation of state.

The sensitivity of the vibrational freezing predictions to the initial flow conditions and to the relaxation model has not been investigated in the present analysis. It is expected that small changes in relaxation parameters can yield large changes in the amount of frozen energy. Furthermore, the presence of impurities such as residual water vapor within the test gas could further alter the relaxation rates and typically delay the onset of vibrational freezing [22, 7] (bringing the two-temperature simulations closer to a thermal equilibrium expansion). High-quality bottled nitrogen (pure to 99.9990%) is used for the Longshot experiments but the remaining species and their potential influence on

DOI: 10.13009/EUCASS2022-6142

the vibrational relaxation rates of nitrogen have not been characterized to date. Hence, large uncertainties exist for the vibrational temperature of the flow and the resulting free-stream conditions. These changes become especially important when considering the possibility of the vibrational energy being relaxed into the flow further downstream as discussed by Boudreau [4]. Validating the presence and amount of frozen energy within the Longshot nozzle flows would require the direct measurement of the free-stream vibrational temperature, possibly using Coherent Anti-Stokes Raman Scattering (CARS) [30]. Such experimental data is not yet available.

The axial distribution of each individual contribution to the flow total enthalpy, as defined in Equation (3), is plotted for both high-temperature cases in Figure 5. At the nozzle inlet, the thermal energy constitutes the vast majority of the total enthalpy of the flow, the remaining being divided between the pressure and temperature corrections. Most of the enthalpy of the flow is then converted into kinetic energy as the flow is expanded through the nozzle, and this exchange occurs very rapidly over the first centimeters of the nozzle expansion. The thermal energy continues to drop further along the nozzle expansion but at a much slower rate until the apex of the test rhombus of the contoured nozzle, located at about $x = 2\,\mathrm{m}$, is reached.

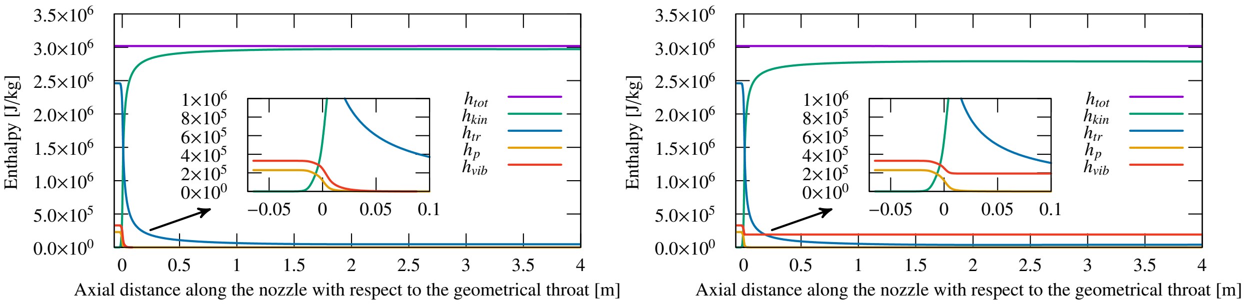

(a) Thermal equilibrium

(b) Two-temperature

Figure 5: Enthalpy components for the two high-temperature models using the excluded volume equation of state.

As expected for the core flow, the sum h_{tot} over all enthalpy contributions remains constant along the nozzle axis, since losses only occur in the boundary layer near the surrounding walls. Because of the symmetry condition imposed along the nozzle axis, the radial velocity component and the heat flux are both zero on the axis, i.e., no radial energy transport takes place. Therefore, all enthalpies must vary through mutual exchange. Due to the decrease in pressure, density and temperature, the vibrational and pressure correction enthalpies must convert to kinetic or translational-rotational enthalpies.

Figure 5a (for a thermal equilibrium flow expansion) shows the vibrational and volume correction enthalpies being converted into kinetic and thermal energy near the nozzle throat. After the expansion, the kinetic energy contribution dominates the total enthalpy. Since the kinetic energy scales with the square of the velocity, any change in the kinetic energy only has a little impact on the flow velocity. On the other hand, only a fraction of the free-stream total enthalpy is thermal energy, meaning that small changes in thermal enthalpy, and thus temperature, have a large impact on the Mach number. The close up in the center of Figure 5a indicates that the enthalpies associated with the high-pressure and high-temperature corrections are essentially negligible beyond the throat. Consequently, the nitrogen gas in the inviscid region of the nozzle quickly approaches its ideal behavior during the initial stages of the expansion.

Using a two-temperature model leads to significant differences, as shown in Figure 5b. There, the vibrational energy freezes shortly after the throat and remains constant for the remaining of the expansion. For the present initial conditions, and with the current relaxation rate model, as much as 6.4 % of the flow total enthalpy is frozen during the expansion, being inaccessible, and yielding free-stream conditions with lower effective enthalpy. The kinetic and thermal enthalpies are both reduced, as can be seen by comparing the translational-rotational thermal enthalpy h_{tr} at $x = 0.1\,\mathrm{m}$ in the close up of the Figures 5a and 5b. The reduced enthalpy impacts the temperature more than the velocity, which leads to an increase of the Mach number with respect to the equilibrium case. The high-pressure correction contribution again rapidly falls to zero, confirming the earlier findings based on the compressibility factor that dense gas effects are limited to the reservoir and throat regions.

3.3 Flow properties along the expansion

The influence of the different numerical models on the flow expansion and the resulting free-stream conditions is well perceived by looking at the Mach number along the nozzle axis, as depicted in Figure 6. The 2019 contoured nozzle of

DOI: 10.13009/EUCASS2022-6142

the Longshot studied herein was designed to yield a uniform Mach 18 flow. The design methodology [13] accounted for the influence of dense gas effects and high-temperature effects (although with a different equation of state [36] than the one considered in this work), yet excluding thermal non-equilibrium effects. The present numerical predictions encompass the design value of the nozzle but none of the results explains the recent experimental flow characterization indicating a Mach number closer to 14 [23] within the free-stream (in-line with the discrepancies reported earlier for similar hypersonic nozzles [4, 16]). Let us first focus on the influence of the high-pressure correction represented by the topmost line in Figures 6a and 6b. There, the Mach number is noticeably larger than for the cases using the ideal gas equation. This is due to the excluded volume equation of state leading to a portion of the reservoir enthalpy being attributed to the pressure term instead of the thermal energy as can be seen in Figure 5a. In particular, the enthalpy which is given by Equation (3), contains the additional term h_p. During the flow expansion, the pressure drops and the pressure-enthalpy is converted to both kinetic and thermal energy, resulting in higher velocities and smaller temperatures. This results in a larger Mach number than in the case of the ideal gas equation. Following the overexpansion of the flow within the nozzle (to Mach numbers larger than the targeted value), the improper cancellation of the characteristic waves leads to a slight recompression that reduces the free-stream Mach number before reaching the nozzle exit.

Unlike the volume correction, the equilibrium approach for the high-temperature correction (bottom curve) causes less expansion, because the vibrational energy relaxes into the translational-rotational thermal energy during the expansion process. This delayed successive introduction of additional thermal energy results in overall higher temperatures. Additionally, the curve is flatter and also monotonically increasing, which indicates that the flow is expanding throughout the nozzle. The nozzle is designed to produce uniform free-stream flow, as can be seen on the basis of the approximately constant Mach number from $x = 2$ onwards for the ideal calorically perfect case in Figure 6a. Since the flow is expanding, the boundary layer grows slower in the equilibrium case. This can be attributed to the increased core flow temperature and therefore pressure, which slightly pushes back the boundary layer. The greater heat capacity at higher temperatures could also lead to a reduction of temperature and pressure for a given enthalpy inside the boundary layer, which could reduce its size. But this does not seem to be the case, since the temperature in the boundary layer is not high enough to contain large amounts of vibrational energy, as shown in Figure 4b.

Employing a two-temperature non-equilibrium model yields Mach numbers slightly below the calorically perfect counterparts, both for the ideal gas equation and the volume correction. The cause is the same effect present in the equilibrium case, but due to the rapid expansion the vibrational energy freezes and thus, the core flow is only heated slightly. Note that even though the free-stream temperature and pressure are lower due to the missing enthalpy the Mach number remains close to the calorically perfect case due to the velocity also being lower.

There seems to be little direct interaction between the high-pressure and the high-temperature models, since the effects simply add up. This results in the volume correction thermal equilibrium Mach number distribution being close to the ideal calorically perfect case. Therefore, if the nozzle flow is in equilibrium, ideal calorically perfect is a reasonable approximation with respect to the Mach number. Nevertheless, it is shown that the use of physically more accurate gas models can have a significant influence on the entire nozzle flow expansion and free-stream quantities.

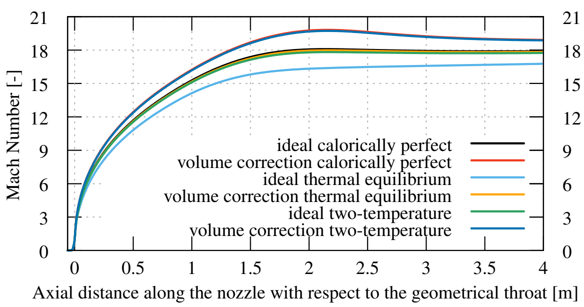

(a) Full nozzle contour

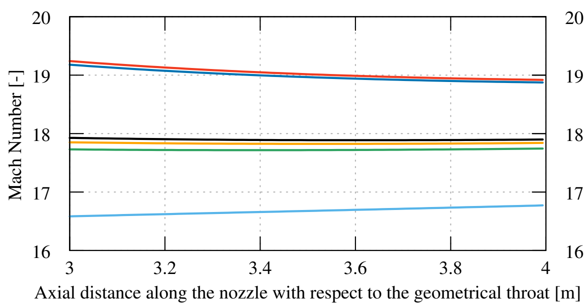

(b) Closeup of the test section. Same key as (a).

Figure 6: Mach number along the nozzle axis for the various gas model combinations.

3.4 Comparison with Pitot pressure measurements

To further demonstrate the discrepancies observed between the numerical prediction and measured quantities, the results from the present simulations are compared in Figure 7 with vertical Pitot pressure profile measurements performed by Kovács et al. [23] for various positions along the nozzle. For the simulations, the Rayleigh-Pitot formula given in

DOI: 10.13009/EUCASS2022-6142

[31] is used to compute the Pitot pressure as a function of the predicted Mach number and static pressure. An ideal gas behavior is required for this equation to hold true. This is justified in the free-stream where low densities and low temperatures are expected. Within the shock layer of the Pitot probe, high-temperature effects could induce slight deviations from the perfect gas assumption that are not accounted for here. We also neglect the influence of vibrational energy in the free-stream and its eventual relaxation across the normal shock. To reduce uncertainties, the influence of thermal non-equilibrium on the change in flow quantities across a shock in front of a measuring probe should be investigated in future works.

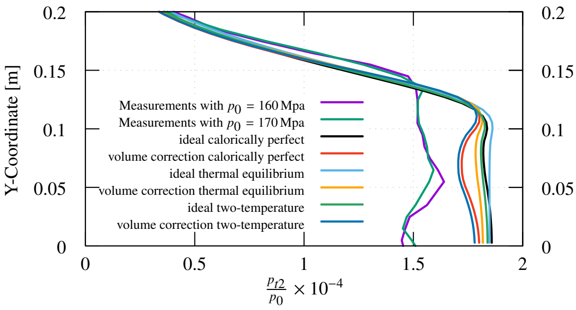

(a) $x = 3.125$ m

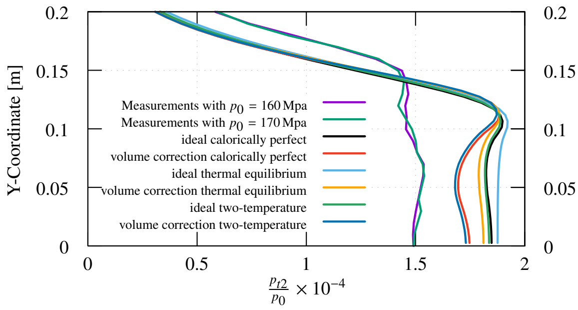

(b) $x = 3.4$ m

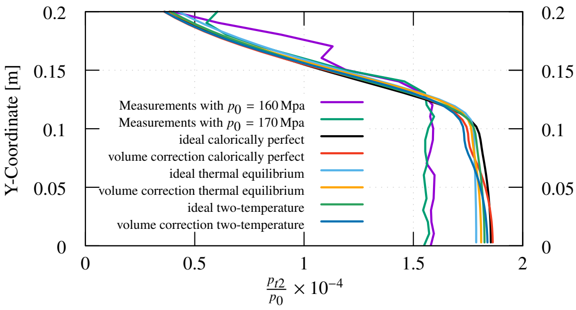

(c) $x = 4.02$ m (nozzle exit)

Figure 7: Pitot pressure profiles for the various gas model configurations. For comparison, vertical pitot pressure measurements performed by Kovács et al. [23] are also included in the plots.

The comparison yields numerical Pitot pressures that are about 20% larger than the experimental values. The trends are similar to the deviations reported in other hypersonic tunnels operating at elevated Mach numbers [5], although the reasons for these deviations are not fully understood.
The overall difference in magnitude can be attributed to the known discrepancy between the measured and computed free-stream conditions. The Pitot pressure is proportional to both Mach number and static pressure, causing the larger computed Mach number to increase and smaller static pressure to decrease the Pitot pressure relative to the measurements. Together, this yields the observed difference in Pitot pressure magnitudes.
Note that the reservoir enthalpies for the experimental data lie between 2.546MJ/kg and 2.883MJ/kg [23], which are lower than the design enthalpy used in this work. Thus, the reservoir and inlet temperatures are correspondingly lower, but still large enough to contain vibrational excitation. Additionally, the flow expansion is rather insensitive to reservoir temperature, because only the non-isentropic parts of the expansion (i.e., viscous effects and the corrections) depend on the reservoir conditions. Therefore, fair comparisons can still be drawn.
The profiles inside the nozzle shown in Figures 7a and 7b exhibit a fluctuation in the core flow profile. This behavior is most pronounced for the volume correction cases, which feature an inwards curved region with lower predicted Pitot pressures, while the measurements show a similar region with higher Pitot pressure.
Comparing the thermal equilibrium case with the other temperature models shows that the thermal equilibrium alleviates the effect. The source of the indented region is a similar region in the static pressure profile, as the Mach number profile remains relatively constant inside the core flow. A possible cause is the chosen gas equation of state, since the volume correction term has a large influence on this effect. Furthermore, the excluded volume equation of state overestimates the high-pressure enthalpy compared to for example the Van der Waals equation, which contains an additional correction constant. For this reason, more advanced high-pressure corrections should be tested to eliminate inaccuracies caused by the current equation of state. However, further extension of the gas equation is unlikely to yield the extreme changes needed for the simulations to match the measurements. This is supported by the fact, that for the

DOI: 10.13009/EUCASS2022-6142

nozzle exit plane profile depicted in Figure 7c where the flow and consequently the Pitot pressure is most uniform, the large discrepancies persist.
Most importantly, all three plots in Figure 7 indicate that the core flow diameter is significantly larger than predicted by the simulations, meaning that the boundary layer growth is overestimated by the current numerical models.

3.5 Boundary layer edge comparison

The boundary layer edge is computed by US3D as the position at which the normalized enthalpy $(h - h_{\text{wall}})/(h_{\text{freestream}} - h_{\text{wall}})$ reaches a value of 0.995. Figure 8 shows the boundary layer edge, which bounds the nozzle core flow region, for all considered gas models. The three plain lines correspond to the different cases relying on a thermally perfect gas equation of state whereas the three dashed lines represent the formulations using the volume correction. The baseline case of the ideal calorically perfect gas yields the largest boundary layer throughout the expansion.

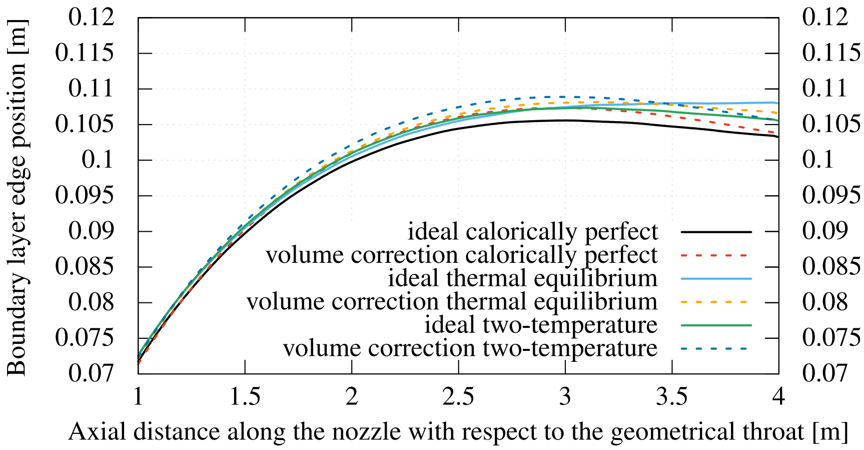

Figure 8: Boundary layer edge, i.e. core flow radius, along a part of the divergent section of the nozzle for the various gas model combinations.

Within the nozzle exit plane ($x = 4$ m), the core flow radii of all test cases vary by at most 5% from each other, as indicated by the large overlap between the individual lines. Hence, the sensitivity of the boundary layer thickness to the gas models employed is rather poor. Yet, none of the numerical models considered here and reported in Figure 8 gets close to the experimental core flow radius, neither within the nozzle, nor within the nozzle exit plane where it should be about 0.15m [23]. This is confirmed by the Pitot pressure comparison (Figure 7), showing that the core flow diameter is severely underestimated by all numerical models.
Next, we compare the boundary layer edge of the ideal calorically perfect baseline, ideal two-temperature and volume correction thermal equilibrium cases, which all have similar free-stream Mach numbers shown by Figure 6. Even though the baseline has the largest Mach number of the three cases, it has the largest boundary layer, see Figure 8. Additionally, at the nozzle exit the ideal gas thermal equilibrium case exhibits the largest core flow radius while it also has the smallest Mach number. For the present cases, the differences in Mach number are mainly due to the differences in the free-stream temperature. Indeed, experimental flow characterization performed by Grossir et al. [14] measured a larger than expected free-stream static pressure and consequently larger temperature as the cause for the large drop in Mach number. It is reasonable to assume that whatever causes the increase in free-stream temperature is also the root cause for the observed large discrepancy of the computed and measured boundary layer thicknesses. Moreover, comparing the core flow radii of the ideal gas calorically perfect, two-temperature and equilibrium cases in Figure 8 shows that the boundary layer is smaller the more heating by vibrational relaxation occurs. This supports the hypothesis that the deviation of the computed boundary layer thickness with respect to the measurements in [23] is due to the same entropy generating heating effect causing the lower Mach number.
A possible mechanism by which the heating causes the reduction in boundary layer thickness is given in the following: Since an increase in temperature is accompanied by an increase in pressure, a heating of the core flow could raise the pressure and consequently push back the boundary layer. A small change in the initial boundary layer thickness can have a large influence on the boundary layer growth and final thickness. Therefore, heating of the flow during early expansion could displace the boundary layer enough to cause the experimentally observed core flow diameter. Even if the underlying cause is different, a phenomenon which increases the free-stream temperature and reduces the boundary layer thickness needs to exist and is not captured by the models investigated in this work.

DOI: 10.13009/EUCASS2022-6142

3.6 Discussion of other influences on the flow expansion

Since the real gas effects that are analyzed in the previous sections fail to reproduce the experimental results, other notable choices in the modelling of the flow expansion are discussed in this section.
First, since the boundary layer thickness is significantly overpredicted by the numerics, the turbulence model is an obvious possible source for the discrepancies. Adding an additional compressibility correction detailed in [34] to the compressible version of the Spalart-Allmaras model decreases the turbulent viscosity, which results in thinner boundary layers. Although the core flow radius can be tuned using this approach, and eventually brought to match the experimental data, it is then associated with a significant decrease of the free-stream static temperature (as a result of the larger flow expansion) and a corresponding increase of the free-stream Mach number. This again contrasts with experimental evidences. It is therefore clear that the turbulence model cannot be the sole cause of the discrepancies and that any turbulence model fitting only amounts to numerical trickery. Therefore, when alleviating the core flow radius deviation by adjusting the turbulence model, the deviation in the Mach number is exacerbated. In other words, the choice of the RANS turbulence model affects only the inviscid contour and can therefore not be the cause of core flow phenomenon. A similar reasoning applies to the wall boundary condition: deviations from the assumed isothermal wall temperature would influence the free-stream flow quantities only through changes in the boundary layer thickness. It is clear that this approach is not effective in explaining the discrepancies.
Another source of uncertainty in the modelling of the flow expansion is the reservoir temperature. This quantity is currently not measured experimentally due to the fast transients and large amplitudes involved. It is instead derived from the set of experimental data, as mentioned in Section 2.4, using the measured reservoir pressure and the free-stream total enthalpy (assuming then an adiabatic nozzle flow). Depending on the gas model used, the temperature can vary quite a lot as seen on the basis of the initial conditions in Table 1. For the ideal gas calorically perfect case, any variation on the reservoir stagnation temperature alters the free-stream static temperature in a similar proportion, but the influence on the free-stream Mach number is weak (being due solely to the different Reynolds number along the nozzle walls that alters the development of the boundary layer). Moreover, a basic investigation performed with lower enthalpies in order to establish comparability with the Pitot pressure measurements, confirms a limited influence of the reservoir temperature on the free-stream flow quantities. Hence, we expect that the range of free-stream conditions that can be achieved while varying the reservoir temperature will lie in the ballpark of the results obtained in this work and shown in the previous sections. This is therefore still not sufficient to explain the discrepancies observed with the experimental data.
Together with the results obtained in Sections 3.2, 3.3 and 3.4 these considerations imply that although the choice of gas model and parameters can significantly influence the flow expansion and free-stream conditions, they are not enough to match the experimental measurements. Therefore, deeper investigations that go beyond the physical models currently available need to be performed. Among the next hypotheses which could be investigated are the one of vibrational relaxation either from foreign species or from free-stream turbulence:

- The first one was suggested by [4], where vibrational freezing would be allowed to relax farther downstream (referred to as a melting phenomenon) once water vapor traces have clustered as a result of flow condensation. No definite proofs for this mechanism seem to have been reported in the literature to date, but numerical results could undoubtedly be brought in closer agreement with experimental data giving the several tuning parameters (vibrational relaxation rates, vibrational melting location and spatial extent) that accompany this hypothesis: the farther away from the throat the melting takes place, the more vibrational energy is converted into thermal energy instead of kinetic energy (hence the larger the influence on the Mach number).

- The second one is that of vibrational relaxation induced by a succession of weak shock waves. The turbulent boundary layers that run along the nozzle walls are indeed responsible for the generation of elevated free-stream turbulence [25, 20] that takes the form of weak shock waves (Mach wavelets) travelling within the flow, as induced by turbulent eddies moving within the boundary layer at supersonic velocities with respect to the boundary layer edge velocity. While a single of these shock waves might not be sufficient to relax all the frozen vibrational energy, a succession of them within a confined environment might behave differently. Since this is an inherently unsteady effect, it is not captured by the RANS simulations performed in this work. Direct Numerical Simulations of Mach 6 nozzle flows [19] and [21] have shown a good agreement with both RANS and experimental data. Whether or not a similar agreement can still be obtained at larger Mach numbers in presence of thermal non-equilibrium effects remains to be demonstrated.

Both effects have the potential to eliminate the observed discrepancies between the simulations and measurements. A key contribution for a better understanding of the flow expansion would be to measure vibrational temperatures by the nozzle exit: a challenging feat within nitrogen flows. Although vibrational frozen energy has recently been measured

DOI: 10.13009/EUCASS2022-6142

in the free-stream of the Mach 18 AEDC Tunnel 9 [10], the different scale and operating conditions of the Longshot could lead to a different behavior that justifies the need for further experimental investigations.

4. Conclusion

In this work we performed a set of RANS simulations of the hypersonic nozzle flow expansion inside the VKI Longshot contoured nozzle. High pressure effects were taken into account by the use of the excluded volume equation of state, while high temperature effects were modeled either by a thermal equilibrium or a two-temperature approach. The resulting axial Mach number distributions are in line with previous predictions, exhibiting significant deviation from the experimental measurements for all cases. The excluded volume equation of state yields larger free-stream Mach numbers than the ideal gas equation. Employing high-temperature corrections reduces the free-stream Mach number, especially for the thermal equilibrium case. A vibrationally frozen flow is predicted by the two-temperature model. Although the real gas corrections are only explicitly important within the convergent and nozzle throat regions, they are necessary for accurate simulations, since the early flow expansion influences the entire flow field. Furthermore, the Pitot pressure and boundary layer edge was compared with recent measurements, showing that the core flow radius is severely underestimated by the present numerical models. The observed discrepancies are attributed to a lack of heating in the core flow, due to non-isentropic effects not captured by the models.

Besides the known Mach number differences, another important quantity with a large discrepancy to the measurements, the boundary layer thickness, is identified. It is particularly useful for model discrimination, since the boundary layer thickness influences the flow expansion and thus the Mach number. Both the Mach number and boundary layer thickness are overestimated by all conducted simulations. Hence, it is shown that the real gas corrections, turbulence models and reservoir conditions cannot solely account for the discrepancies between the numerical and experimental free-stream conditions.

The need for further numerical and experimental investigations of the nozzle flow expansion has been established. In future work, vibrational relaxation rate calculations, taking water vapor condensation into account, are of interest. Direct numerical simulations would be beneficial to characterize the effect of turbulent weak shock waves on the flow expansion and on the thermal non-equilibrium. Measurements with a monoatomic gas or direct measurement of the free-stream vibrational temperature are of interest, since they could provide insight on the accuracy of the two-temperature approach.

Acknowledgments

This material is based upon work supported by the Air Force Office of Scientific Research under award number FA8655-20-1-7024.

References

[1] J. Ahrens, B. Geveci, and C. Law. Paraview: An end-user tool for large data visualization. *The visualization handbook*, 717(8), 2005.

[2] J.D. Anderson. *Hypersonic and High Temperature Gas Dynamics*. McGraw-Hill series in aeronautical and aerospace engineering. American Institute of Aeronautics and Astronautics, 2000.

[3] F.G. Blottner, M. Johnson, and M. Ellis. Chemically reacting viscous flow program for multi-component gas mixtures. Technical Report SC-RR-70-754, Sandia Labs., Albuquerque, N. Mex., 1971.

[4] A.H. Boudreau. Characterization of flow fields in hypersonic ground test facilities. *Methodology of Hypersonic Testing, Lecture Series*, 3:4–1, 1993.

[5] G.V. Candler. Hypersonic nozzle analysis using an excluded volume equation of state. In *38th AIAA Thermophysics conference*, number AIAA paper 2005-5202, June 2005.

[6] G.V. Candler, H.B. Johnson, I. Nompelis, V.M. Gidzak, P.K. Subbareddy, and M. Barnhardt. Development of the us3d code for advanced compressible and reacting flow simulations. In *53rd AIAA Aerospace Sciences Meeting*.

[7] G.V. Candler and K. McConaughey. Effect of water vapor on the AEDC tunnel 9 Mach 14 nozzle flow. In *47th AIAA Aerospace Sciences Meeting including The New Horizons Forum and Aerospace Exposition*. January 2009.

DOI: 10.13009/EUCASS2022-6142

[8] S. Catris and B. Aupoix. Density corrections for turbulence models. *Aerospace Science and Technology*, 4(1):1–11, 2000.

[9] J.D. Cox, D.D. Wagman, and V.A. Medvedev. *CODATA Key Values for Thermodynamics*. New York. Hemisphere Publishing Corp, 1984.

[10] A. Dogariu, L.E. Dogariu, M.S. Smith, B. McManamen, J.F. Lafferty, and R.B. Miles. Velocity and temperature measurements in Mach 18 nitrogen flow at Tunnel 9. In *AIAA Scitech 2021 Forum*.

[11] L. Eça and M. Hoekstra. A procedure for the estimation of the numerical uncertainty of CFD calculations based on grid refinement studies. *Journal of Computational Physics*, 262:104–130, 2014.

[12] G. Grossir. *Longshot Hypersonic Wind Tunnel Flow Characterization and Boundary Layer Stability Investigations*. PhD thesis, von Karman Institute for Fluid Dynamics-Université Libre de Bruxelles, 2015.

[13] G. Grossir. Design of axisymmetric contoured nozzles for calorically and thermally imperfect gases using the Hypnoze code. In *HiSST: 2nd International Conference on High-Speed Vehicle Science & Technology*, number 2022-0038, September 2022.

[14] G. Grossir and B. Dias. Flow characterization of the VKI Longshot wind tunnel. In O. Chazot and G. Grossir, editors, *Flow characterization and modeling of hypersonic wind tunnels*, volume VKI Lecture Series 2018/19, chapter 3. von Karman Institute for Fluid Dynamics, December 2018.

[15] G. Grossir, Z. Ilich, and O. Chazot. Modeling of the VKI Longshot gun tunnel compression process using a quasi-1D approach. In *33rd AIAA Aerodynamic Measurement Technology and Ground Testing Conference*, number AIAA paper 2017-3985, June 2017.

[16] G. Grossir, S. Paris, P. Rambaud, and B. Van Hove. Design of static pressure probes for improved free-stream characterization in hypersonic wind tunnels. In *52nd AIAA Aerospace Sciences Meeting*, number AIAA paper 2014-1410, January 2014.

[17] G. Grossir, B. Van Hove, S. Paris, P. Rambaud, and O. Chazot. Free-stream static pressure measurements in the Longshot hypersonic wind tunnel and sensitivity analysis. *Experiments in Fluids*, 57(64):1–13, May 2016.

[18] W.M. Haynes, D.R. Lide, and T.J. Bruno. *CRC Handbook of Chemistry and Physics*. CRC press, 2014.

[19] N. Hildebrand, M.M. Choudhari, and L. Duan. Direct numerical simulations of acoustic disturbances in various rectangular nozzle configurations. In *AIAA Scitech 2020 Forum*.

[20] N. Hildebrand, M.M. Choudhari, and L. Duan. Direct Numerical Simulations of acoustic disturbances in various rectangular nozzle configurations. In *AIAA Scitech*, number AIAA paper 2020-0587, January 2020.

[21] J. Huang and L. Duan. Direct numerical simulation of acoustic noise generation from the nozzle wall of a hypersonic wind tunnel. In *47th AIAA Fluid Dynamics Conference*.

[22] V. Joly and C. Marmignon. Effect of H_2O vapor on the vibrational relaxation in hypersonic wind tunnels. *Journal of Thermophysics and Heat Transfer*, 11(2):266–272, 1997.

[23] D.G. Kovács, Z. Ilich, G. Grossir, and O. Chazot. Experimental characterization of the VKI Longshot Mach 14 contoured nozzle. In *AIAA SCITECH 2022 Forum*. 2022.

[24] E.M. Kraft. After 40 years why hasn't the computer replaced the wind tunnel? *ITEA journal*, 31:329–346, 2010.

[25] J. Laufer. Sound radiation from a turbulent boundary layer. Technical Report TR-32-119, Jet Propulsion Laboratory, California Institute of Technology, November 1961.

[26] MATLAB. *version 9.12.0 (R2022a)*. The MathWorks Inc., Natick, Massachusetts, 2022.

[27] R.C. Millikan and D.R. White. Systematics of vibrational relaxation. *The Journal of Chemical Physics*, 39(12):3209–3213, 1963.

[28] C. Park, J.T. Howe, R.L. Jaffe, and G.V. Candler. Review of chemical-kinetic problems of future NASA missions. II - Mars entries. *Journal of Thermophysics and Heat Transfer*, 8(1):9–23, 1994.

DOI: 10.13009/EUCASS2022-6142

[29] R.W. Perry. The Longshot type of high-Reynolds number hypersonic tunnel. In *Third hypervelocity techniques symposium*, Advanced experimental techniques for study of hypervelocity flight, March 1964.

[30] B.D. Prince, A. Chakraborty, B.M. Prince, and H.U. Stauffer. Development of simultaneous frequency- and time-resolved Coherent Anti-Stokes Raman scattering for ultrafast detection of molecular Raman spectra. *The Journal of Chemical Physics*, 125(4):044502, 2006.

[31] Ames research staff. Equations, tables, and charts for compressible flow. Technical Report NACA-TR-1135, NASA, 1953.

[32] P.J. Roache. Perspective: A Method for Uniform Reporting of Grid Refinement Studies. *Journal of Fluids Engineering*, 116(3):405–413, 09 1994.

[33] J.B. Scoggins, V. Leroy, G. Bellas-Chatzigeorgis, B. Dias, and T.E. Magin. Mutation++: MUlticomponent Thermodynamic and Transport properties for IONized gases in C++. *SoftwareX*, 12:100575, 2020.

[34] P. Spalart. Trends in turbulence treatments. In *Fluids 2000 Conference and Exhibit*. 2000.

[35] P. Spalart and S. Allmaras. A one-equation turbulence model for aerodynamic flows. In *30th Aerospace Sciences Meeting and Exhibit*. 1992.

[36] R. Span, E.W. Lemmon, R.T. Jacobsen, W. Wagner, and A. Yokozeki. A reference equation of state for the thermodynamic properties of nitrogen for temperatures from 63.151 to 1000K and pressures to 2200MPa. *Journal of Physical and Chemical Reference Data*, 29(6):1361–1433, 2000.

[37] E. Tiesinga, P. Mohr, D. Newell, and B. Taylor. CODATA recommended values of the fundamental physical constants: 2018. (93), 2021-06-30 04:06:00 2021.

[38] T. Williams, C. Kelley, and many others. Gnuplot 5.2: an interactive plotting program. http://gnuplot.sourceforge.net/, 2021.